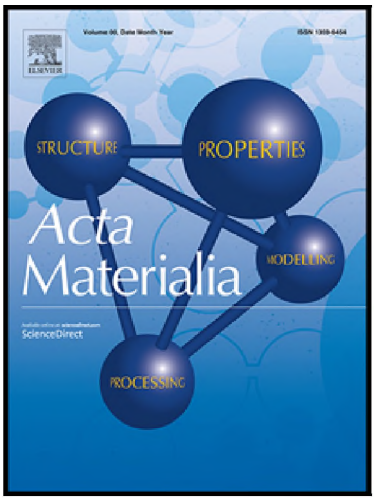

Domain Wall Motion Across Microstructural Features in Polycrystalline Ferroelectric Films

Gavin Hennessey , Travis Peters , Pannawit Tipsawat , Marti Checa , Liam Collins , Susan Trolier-McKinstry

PII: S1359-6454(23)00202-1
DOI: https://doi.org/10.1016/j.actamat.2023.118871
Reference: AM 118871

To appear in: *Acta Materialia*

Received date: 19 December 2022
Revised date: 27 February 2023
Accepted date: 18 March 2023

Please cite this article as: Gavin Hennessey , Travis Peters , Pannawit Tipsawat , Marti Checa , Liam Collins , Susan Trolier-McKinstry , Domain Wall Motion Across Microstructural Features in Polycrystalline Ferroelectric Films, *Acta Materialia* (2023), doi: https://doi.org/10.1016/j.actamat.2023.118871

Notice of Copyright

Domain Wall Motion Across Microstructural Features in Polycrystalline Ferroelectric Films

Gavin Hennessey[a], *Travis Peters*[a], *Pannawit Tipsawat*[a], *Marti Checa*[b], *Liam Collins*[b], *and Susan Trolier-McKinstry*[a]

[a] Materials Science and Engineering Department and Materials Research Institute, The Pennsylvania State University, University Park, Pennsylvania 16802, United States

[b] Center for Nanophase Materials Science, Oak Ridge National Laboratory, Oak Ridge, Tennessee 37831, United States

Corresponding Author: Travis Peters[a], Email: tlp5454@psu.edu, Phone number: 1 + (419) 551-4207, Postal Address: Millennium Science Complex, N-225-2, University Park, PA 16802, United States

Keywords: Piezoelectricity, Atomic force microscopy, Electron backscatter diffraction, Nonlinear, Correlated wall motion

Abstract

This paper describes the effect of microstructural features such as grain boundaries and triple points on the pinning of domain wall motion in perovskite $Pb(Zr_{0.52}Ti_{0.48})O_3$ (PZT) films on polycrystalline $SrRuO_3/SrTiO_3$ substrates. Spatial variability in the collective domain wall dynamics was assessed using non-linearity mapping via Band Excitation Piezoresponse Force Microscopy (BE-PFM). Collocating the non-linearity maps with triple point locations (as visualized by EBSD) allowed for exploration of the effects that local microstructure (e.g., grain boundary) have on domain wall motion. It was found that the extrinsic behavior varied with both the misorientation angle and the proximity to the grain boundary. The width of influence of individual grain boundaries on the motion of domain walls was a function of the character of the grain boundary; random grain boundaries exhibit deeper minima in $\alpha_d/d_{33,initial}$ and larger widths of influence (up to 905 nm) compared to coincident site lattice (CSL) boundaries (up to 572 nm). Additionally, triple points containing larger numbers of random boundaries exhibited non-Rayleigh behavior to greater distances, suggesting that the triple point provides either a deep potential minimum or a region where domain wall motion is unfavorable.

1. Introduction

The piezoelectric response of ferroelectric materials can be divided into intrinsic and extrinsic sources, where the intrinsic response corresponds to the appropriate average of the single domain single crystal response; extrinsic contributions are those due to motion of mobile interfaces such as phase boundaries or domain walls [1–5]. The macroscopic properties of polycrystalline perovskites are the ensemble average of many grains and even more domain walls. Calculating the response of ceramics, however, is challenging due to the grain-to-grain coupling, the interactions between the intrinsic and extrinsic contributions, the inherent anisotropy of the

piezoelectric response, and incomplete knowledge about how local elastic and electric fields influence domain wall motion. It is thus interesting to explore somewhat simplified systems where the effect of single factors on extrinsic contributions can be quantified. This paper focuses on the characteristics of individual grain boundaries and triple points on the extrinsic piezoelectric response in lead zirconate titanate (PZT) films, as a model system.

Extrinsic contributions have been reported to decrease near grain boundaries in ferroelectric films and ceramics. Randall et al. demonstrated that the piezoelectric properties of PZT ceramics decreased with decreasing grain size, which was attributed to a change in the domain structure and a reduction in domain wall contributions [6]. Similarly, Griggio et al. reported that an average grain size increase from 110 nm to 270 nm in PZT-based films was accompanied by a doubling of the irreversible dielectric Rayleigh coefficient α_d from 5.3 ± 0.1 cm/kV to 10.6 ± 0.1 cm/kV [7]. α_d is associated with the irreversible motion of domain walls. Grain boundaries have also been reported to influence the ferroelectric switching characteristics [8–11].

Marincel et al. measured the local impact of single grain boundaries on the irreversible to the reversible Rayleigh coefficient ratios using band excitation piezoresponse force microscopy (BE-PFM). Both reversible $d_{33,initial}$ and irreversible, α_d, Rayleigh coefficients were calculated from the nonlinear dependence of out-of-plane deflection on increasing applied AC voltage. The ratio of $\alpha_d/d_{33,initial}$ suggested increased pinning of domain wall motion within 476 nm of a 24 ° tilt grain boundary in a $PbZr_{0.52}Ti_{0.48}O_3$ (PZT 52/48) film on a bicrystal substrate [12]. The width of influence of the reduced response at grain boundaries was found to be dependent on both the misorientation angle and the tilt/twist characteristics of the boundary [13].

Among the factors thought to affect the width of influence of a particular grain boundary is the connectivity of the domain structure across the structural discontinuity. Following seminal work

by Tsurekawa [14], Mantri reported that for random grain-grain misorientations, domain continuity is dependent on the ability of the material to compensate strain mismatch and minimize the polarization charge at the grain boundary [15]. It was found that a larger uncompensated charge and/or bigger spontaneous polarizations make continuity less energetically favorable.

Fousek et al. studied permissible orientations of ferroelectric domain walls in detail. He noted that uniform strain states should in theory only yield domain walls along planes of mechanical compatibility in the absence of external stress [16]. When no additional elastic strain develops, the domain wall is deemed a "permissible wall" [16]. If two non-permissible domains meet along a stressed boundary, domain switching is expected to be restricted, as has been noted in grain boundary pinning [16,17]. The domain structure is thus a developing system that acts in response to strain and charge from differently oriented polarizations.

To date, quantitative evaluations of the role of individual grain boundaries on the motion of domain walls are limited, with most of the data pertaining to symmetrical grain boundaries. A more comprehensive set of data is required to better understand the role that grain boundaries exert in pinning extrinsic contributions to the properties. It is speculated that grain boundaries with a shared axis rotation, i.e., Coincident Site Lattice (CSL) boundaries, may facilitate domain wall motion across the grain boundary relative to random grain boundaries. Thus, in this work, the intrinsic and extrinsic contributions to the piezoelectric response were assessed for PZT films deposited onto polycrystalline large-grained $SrRuO_3/SrTiO_3$ substrates. The substrates allowed many grain boundary orientations to be isolated by Electron Backscatter Diffraction (EBSD) and categorized based on grain boundary angle and shared orientation axes. BE-PFM imaging was used to quantify the local piezoelectric nonlinearities.

2. Experimental Procedure

Strontium titanate ($SrTiO_3$) ceramic substrates, obtained from Knowles Precision Devices, were cleaned, mechanically polished, and annealed prior to depositing the strontium ruthenate ($SrRuO_3$) bottom electrodes. The final substrate polishing parameters and anneal conditions are given in Supplemental Materials. Epitaxial $SrRuO_3$ bottom electrodes were deposited on the $SrTiO_3$ substrates by pulsed laser deposition (PLD) following the conditions listed in Table S1 in Supplemental Materials. The detailed procedure for $SrRuO_3$ deposition via PLD is also given in Supplemental Materials.

The samples were cleaned with acetone, ethanol, and isopropyl alcohol, then annealed at 750°C for 1 min in a rapid thermal annealer (Allwin21 Corp AW 810 RTP). A modification of the processes reported by Borman and Zhu was used for chemical solution deposition of the PZT films [18,19]. A Mitsubishi Materials Corporation 114/52/48/2 PZTNb solution of $PbZr_{0.52}Ti_{0.48}O_3$ with 14 mol% excess Pb and 2 mol% Nb was utilized for PZT film growth. Sol-gel PZT deposition conditions are given in Supplemental Materials.

Layers of LOR 5A (Microchem) and SPR3012 (Dow Electronic Materials) photoresist were spin coated, soft-baked, then exposed at 180 mJ/cm^2 using 405 nm laser MLA150 advanced maskless aligner (Heidelberg, Germany). The exposed areas of patterned resist were circles with a diameter of 200 μm. MF CD-26 developer (1-5% Tetramethylammonium hydroxide (TMAH) in water – Dow Electronic Materials) was then utilized to develop the exposed photoresist areas and reveal the underlying PZT. An oxygen plasma ash step using an M4L RF Gas Plasma System (PVA TePla Corona, California) with gas flow rates of 50 sccm He and 150 sccm O_2, at a pressure of 550 mTorr, and an RF power of 200 W for 1 min then served to remove any remaining resist in the patterned areas.

Electron Backscatter Diffraction (EBSD) was used to analyze the films for crystallographic orientations and grain boundary locations, as demonstrated in Figure S1 in Supplemental Materials. The angle between any two grains was calculated using the Aztec crystal software. Crystallographic orientation of the 200 μm diameter lithographically defined circular electrode area was mapped before top electrode deposition, as shown in Figure S2 (a,b) in Supplemental Materials. Top platinum electrodes 50 nm thick were sputter deposited (Kurt Lesker CMS-18, Pittsburgh PA) with an Ar chamber pressure of $2.5x10^{-3}$ Torr at room temperature. The plasma was struck through the application of 200 W DC. Post-deposition photoresist lift-off resulted in circular top electrodes for electrical measurements. Finally, to improve adhesion of the top electrode to the PZT surface, each sample underwent an RTA step at 550 °C for 1 min with a heating rate of 4 °C/s and ambient chamber conditions (no gas flow).

Using a secondary photolithography step, a set of crosshairs was created around the platinum electrodes to act as cardinal directions for PFM scan alignment, shown in Figure S2 (a,c) in Supplemental Materials. Square bonding pads were also added during this step, as shown in Figure S2c. Approximately 200 nm of gold was sputtered onto the exposed areas of each sample (Kurt Lesker CMS-18, Pittsburgh PA) using a power supply setpoint of 200 W and a chamber pressure of 4.7 mTorr at 22°C for 400 seconds.

BE-PFM [20] was performed using a commercial atomic force microscope (AFM), namely a Cypher AFM (Asylum Research an Oxford Instruments Company, Santa Barbara, CA) equipped with PXI architecture, based on National Instruments NI-6124 fast arbitrary waveform generator and data acquisition cards controlled using custom labview software. All measurements were performed using Pt/Ir-coated cantilevers (BudgetSensors Multi75E-G) with a nominal spring constant of ~3 N/m and resonance frequency of ~75 kHz. Quantitative local measurements of

piezoelectric nonlinearity in the Rayleigh regime were acquired via nonlinear BE-PFM, as previously described [21]. Nonlinear BE-PFM experiments were conducted by varying the excitation amplitude from 0 to ~1/2 the coercive voltage in the frequency range of 300 to 400 kHz, around the contact resonance of the probe. To separate material non-linearities from cantilever non-linearities, the AC driving voltage was swept up and down in frequency, and the phase content of the chirp wave was adjusted to keep the cantilever dynamics in the linear regime, as described previously [22]. The deflection amplitude as a function of frequency was fit to a simple harmonic oscillator (SHO) model and the amplitude at resonance (A_{max}), resonance frequency and Q factor were extracted for each applied AC electric field (E_{AC}). Spectral images were collected on a dense grid of points on the top electrode, providing a 3-dimensional dataset containing information on spatial (x,y) and E_{AC} dependence, A_{max} (x,y,E_{AC}). Spatial maps of the Rayleigh coefficients were extracted by fitting A_{max} vs E_{AC}, for each spatial location, with a second order polynomial $A_{max}=A2*E_{AC}+A3*E_{AC}^2$, where $d_{33,initial} \propto A2$ and $2*A3 \propto \alpha_d$.

Prior to BE-PFM measurements, the samples were poled at three times the coercive field at 150°C for 15 minutes. Care was taken to ensure that the piezoelectric phase was uniform across the scan area. Using the EBSD map, several triple points which contained a varying number of random and coincident site lattice grain boundaries were located. From BE-PFM, the piezoresponse amplitudes varied between grains, as expected, due to their different grain orientations. BE-PFM nonlinearity measurements were acquired within a scan area of either 4x4 μm^2 measuring 80x80 $pixels^2$ or 5x5 μm^2 with 100x100 $pixels^2$, keeping the pixel separation constant at 50 nm (on the order of magnitude of the probe radius). EBSD orientation and PFM Rayleigh ratio ($\alpha_d/d_{33,initial}$) maps were correlated with respect to each other, aided using the fiduciary marks, which enabled the direct comparison of $\alpha_d/d_{33,initial}$ responses at and around

precise grain boundary locations of interest. Individual grains were color-coded with respect to the orientation key in all EBSD maps.

3. Results & Discussion

A method adopted from Marincel et al. (Method 3), which utilize clustered response behavior, were implemented to analyze the width of influence of individual grain boundaries on the motion of domain walls [12]. In particular, the average nonlinear response was calculated parallel to the grain boundary in 50 nm (BE-PFM pixel size) increments away from the boundary as the distance from grain boundary. The average and standard deviation of the nonlinear response in each grain was then determined far from the grain boundary, where the $\alpha_d/d_{33,initial}$ appeared to be independent of the distance from the boundary. The width of influence was determined from the collective nonlinear response of the grain far from the grain boundary. The width of influence standard deviation was calculated as 25% of the standard deviation of each grain's nonlinear response. Given the different orientations of the grains, a separate mean and standard deviation for each grain were collected on both sides of each grain boundary. The following discussion describes several triple point regions in the film and characterizes their response.

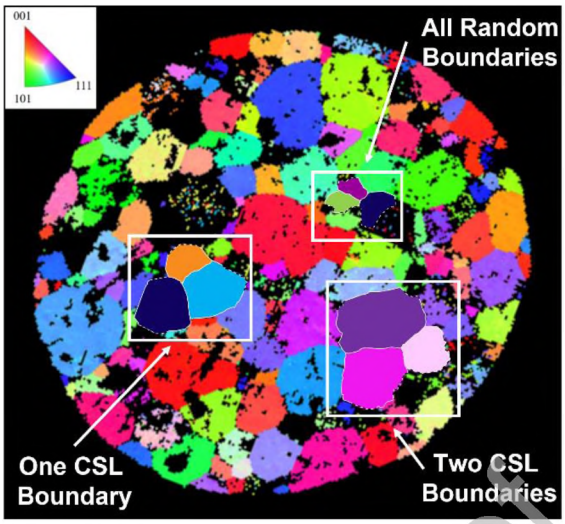

Figure 1: EBSD orientation map of the capacitor structure with the three triple points under investigation highlighted. Also shown is the crystallographic orientation color map (top left corner).

The capacitor used in this investigation is displayed in the EBSD map in Figure 1. A sample tilt of 70° during SEM and EBSD measurements resulted in the circular electrode appearing eliptical. The three triple points highlighted were selected for investigation based on having a different number of CSL vs random boundaries. The selected triple points exhibit two CSL, one CSL, and entirely random boundaries.

The first triple point investigated corresponds to the map in Figure 2a with two CSL boundaries and one random boundary present. For the following analysis, the lower left grain will be referred to as fuchsia, the lower right grain as pink, and the top grain as purple, where the color was assigned based on the EBSD grain orientation. The location of the PFM scan region is the white box at the triple point of these three grains. The topography of the 5x5 μm^2 scan size is displayed in Figure 2b, showing a relatively smooth electrode with a few large (> 30 nm) contamination features. The BE-PFM $\alpha_d/d_{33,initial}$ map of the approximate 5x5 μm^2 region is

shown in Figure 2c. Here, the large topographic artifacts display a piezoelectric response with a negative A3 coefficient, indicative of non-Rayleigh like behavior. Outside of the artifacts, there are distinct regions of high nonlinear response in the grains and lower responses near the grain boundaries, which are indicated by white lines in Figure 2c. Figure S3 in Supplemental Materials shows the quadratic A2 coefficient and A3 coefficient maps.

The average response vs. grain boundary position for the three grain boundaries is shown in Figure 2 d-f. Figure 2d shows the results for the purple-fuchsia 60.9° CSL grain boundary, which displays a pinning influence that stretches 379 ± 76 nm into the purple grain and 193 ± 295 nm into the fuchsia grain for a total width of influence of 572 ± 371 nm. The thicker horizontal red dotted line represents the average $\alpha_d/d_{33,initial}$ far from the boundary, and the other two red dotted lines represent 25% of the standard deviation away from that mean; the black vertical dotted line marks the Σ17b grain boundary. The fuchsia grain has an average $\alpha_d/d_{33,initial}$ that goes through a shallow maximum of $1.4x10^{-3} \pm 0.5x10^{-4}$ cm/kV (error is 25% of the grain response standard deviation) while the purple grain has an average $\alpha_d/d_{33,initial}$ that reaches a larger steady state value of $3.5x10^{-3} \pm 0.1x10^{-3}$ cm/kV. The vertical purple and pink lines indicate the respective pinning distances away from the grain boundary, and the distance between the colored vertical lines is labeled with the entire grain boundary width of influence.

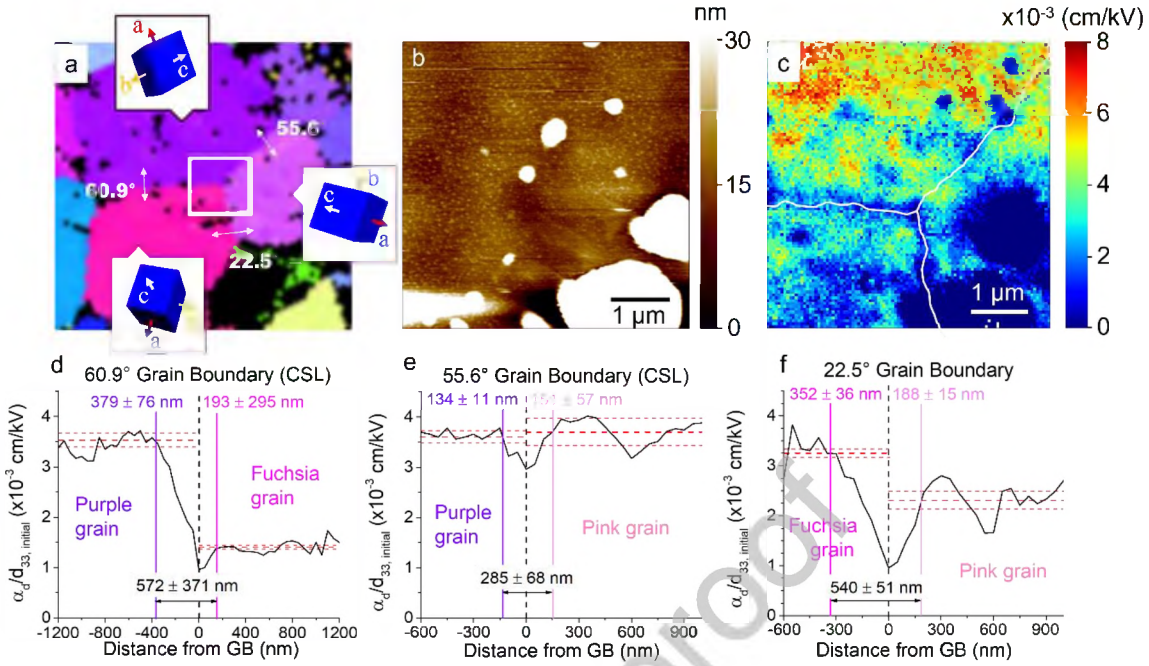

Figure 2: Analysis of the grain boundaries separating purple, pink, and fuchsia grains. (a) EBSD schematic of the three grains with each grain boundary misorientation angle labeled, the crystallographic orientation of each grain is shown, and approximate size of the BE-PFM scan given within the white box. (b) Contact mode AFM scan of a 5x5 μm^2 region around the triple point. (c) BE-PFM nonlinear $\alpha_d/d_{33,initial}$ Rayleigh ratio spectroscopic map showing the relative magnitude of domain wall mobility. White lines are overlaid on the grain boundary regions. (d-f) Average $\alpha_d/d_{33,initial}$ ratios with respect to grain boundary proximity for (d) fuchsia/purple 60.9° grain boundary, (e) purple/pink 55.6° grain boundary and (f) fuchsia/pink 22.5° grain boundary. The grain boundaries are marked as the center dashed black vertical lines, the thick red horizontal dashed lines represent an average $\alpha_d/d_{33,initial}$ far from the grain boundary. Thinner dashed red lines mark 25% of the standard deviation from the mean grain response, and the domain wall pinning distance into each grain, along with the total grain boundary width of influence, are labeled.

For comparison, the 55.6° boundary that separates purple and pink is a Σ3 CSL boundary, as shown in Figure 2e. The purple grain reaches a steady state $\alpha_d/d_{33,initial}$ value of $3.6x10^{-3} \pm 0.1x10^{-3}$ cm/kV away from this pink-purple boundary. This is similar to the average response of the purple grain away from the purple/fuschia boundary, though the local minimum of $3.0x10^{-3}$ cm/kV at the grain boundary position in purple-pink exceeds the $0.9x10^{-3}$ cm/kV minimum for the fuchsia-purple boundary. This result suggests stronger local pinning (or a lower density of domain walls) for the Σ17b 60.9° grain boundary. The width of influence is also found to be greater for the 60.9° boundary, despite similar steady state behavior far into the grain from both grain boundaries. Steady state behavior in the purple grain for the 55.6° boundary occurs at 134 ± 11 nm from the grain boundary, compared to 379 ± 76 nm for the 60.9° grain boundary.

Considering just these two coincident site lattice boundaries, the larger degree of misorientation and deeper minima led to an increased width of influence on domain wall motion; however, as is shown in Figure 2f, this is not always the case. The final boundary of this triple point is the fuchsia-pink boundary, displayed in Figure 2f. This is a random boundary (not CSL) with a misorientation angle of 22.5°. Relatively symmetric behavior can be seen on either side of the boundary up to ~ 150-200 nm. Beyond this distance, neither the pink nor the fuchsia grain reached the same average $\alpha_d/d_{33,initial}$ as the CSL boundaries. While the reason for this is not fully known, it is speculated that differences in the domain structures across a grain may depend on the matching conditions across the adjacent grain boundary. It should be noted that of the three grain boundaries intersecting at this triple point, the random grain boundary demonstrated the deepest minima in $\alpha_d/d_{33,initial}$ at the grain boundary position. Random grain boundaries were found to exhibit the largest total width of influence and deepest minima in $\alpha_d/d_{33,initial}$.

A large number of topographical defects notably induced a dip in $\alpha_d/d_{33,initial}$ some 500 nm into the pink grain. Despite these points being eliminated from the averages, the $\alpha_d/d_{33,initial}$ ratios of the surrounding material may be affected; a distribution of strong pinning sites may drive variability in the average $\alpha_d/d_{33,initial}$ maps adjacent to these points.

The pinning influence of the 22.5° boundary, shown in Figure 2f, was estimated to stretch 352 ± 36 nm into the fuchsia grain and 188 ± 15 nm into the pink grain for a total width of influence of 540 ± 51 nm. The larger individual width of influence for both the fuchsia and pink grains were found in the random grain boundary compared to the CSL boundary. This trend of CSL boundaries pinning less than random boundaries held true for all the investigated triple points; the largest triple point width of influence appears in the cases where more random boundaires are present. The only exception to this arises in the case of the two boundaries involved with the pink grain. The unique response of the 22.5° and 55.6° boundaries are thought to be connected to the large topological features which influenced neighboring measurements deep into the pink grain, despite the removal of affected $\alpha_d/d_{33,initial}$ data when calculating averages.

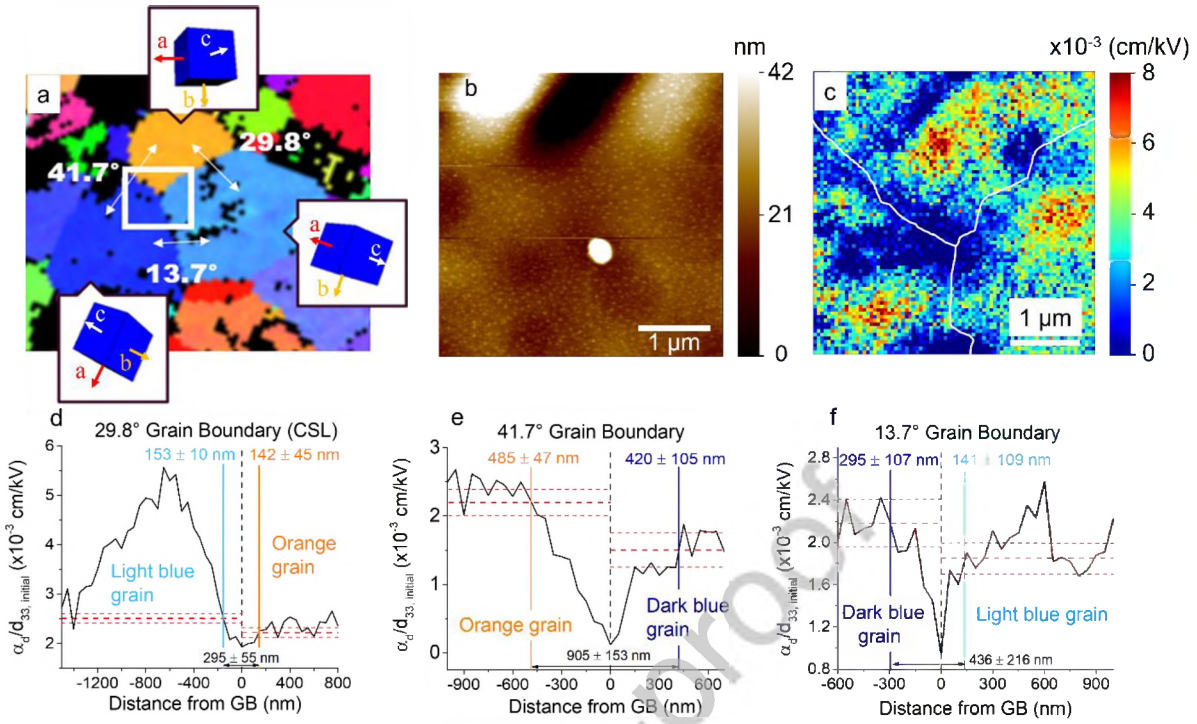

Figure 3: Analysis of the three grain boundaries separating the light blue, dark blue, and orange grains. (a) Schematic of the triple point. (b) Contact AFM scan of a 4x4 μm^2 region around the triple point. (c) BE-PFM Rayleigh ratio spectroscopic map of the same approximate region. (d-f) Average Rayleigh ratio $\alpha_d/d_{33,initial}$ with respect to the grain boundary position for (d) the light blue/orange 29.8^o grain boundary, (e) the orange/dark blue 41.7^o grain boundary, and (f) the dark blue/light blue 14.7^o grain boundary.

The second triple point within this investigation contained only a single CSL grain boundary. For the orange - light blue - dark blue triple point, the CSL grain boundary was between the light blue and orange grains, displaying a misorientation angle of 29.8 ° which corresponds to a rotation around {111}. Figure 3a shows the EBSD schematic of all three grains with each Euler angle and approximate grain orientation. Figure 3b shows the 4x4 μm^2 contact AFM scan around the triple point, and Figure 3c shows the local nonlinear Rayleigh ratios in the same region.

Figure S4 in Supplemental Materials shows the individual PFM quadratic A2 and A3 coefficients. It should be noted that the 29.8° CSL boundary had both the shallowest minima and lowest width of influence for this triple point: 295 ± 55 nm, which is shown in Figure 3d. The largest reported influence in this investigation was 905 ± 152 nm for the random 41.7° boundary within the same triple point, shown in Figure 3e. The 41.7° boundary had a relatively asymmetric response. It is notable that the minima was more than an order of magnitude different between the dark blue-orange ($\alpha_d/d_{33,initial}$ value of $0.12x10^{-3}$ cm/kV) and light blue-orange ($\alpha_d/d_{33,initial}$ value of $1.9x10^{-3}$ cm/kV) grain boundaries. Steady state was approached at 485 ± 47nm and 420 ± 105 nm into the orange and dark blue grains, respectively. The total width of influence for the dark blue-orange grain boundary was therefore 905 ± 152 nm. In some cases, random grain boundaries demonstrated a width of influence of ~ 1 μm, while the largest recorded CSL boundary influence of all the triple points was 572 ± 371 nm. The final random 13.7° boundary that separated dark blue and light blue is shown in Figure 3f. Like the other reported random boundaries, it was found to exhibit more symmetric $\alpha_d/d_{33,initial}$ behavior near the boundary than the adjacent CSL light blue-orange grain boundary. Similar to the purple-pink-fuchsia triple point region, the random boundaries exhibited deeper minima of $\alpha_d/d_{33,initial}$ compared to their associated CSL boundary neighbors. The light and dark blue areas reached their steady state at 141 ± 109 nm and 295 ± 107 nm into the grain, respectively, for a total width of influence of 436 ± 216 nm.

Uncovering local structural features tied to decreased pinning is also fundamental to this work; it is shown here in the case of the green-blue-pink triple point consisting of entirely random boundaries as is displayed in Figure 4. Despite the presence of a 45.1 ° grain boundary, shown in

Figure 4d, no evidence of pinning correlates with proximity to the blue-pink grain boundary. Instead, a minimum is found some 500 nm into the pink grain.

All three blue-pink-green boundaries show $\alpha_d/d_{33,initial}$ minima at the grain boundary an order of magnitude smaller than the others. Again, the individual A2 and A3 (associated with $d_{33,initial}$ and α_d, respectively) quadratic coefficients are given in Figure S5 in Supplemental Materials. Additionally, all three of the boundaries in this region correspond to random boundaries. This has been correlated with the deepest pinning levels of all three triple points in this investigation. It is thought that a triple point of three random boundaries may exacerbate this finding and contribute to low reported $\alpha_d/d_{33,initial}$ minima and comparatively large widths of influence. The 37.8° blue-green boundary, shown in Figure 4e, had the second largest total influence, at 859 ± 186 nm.

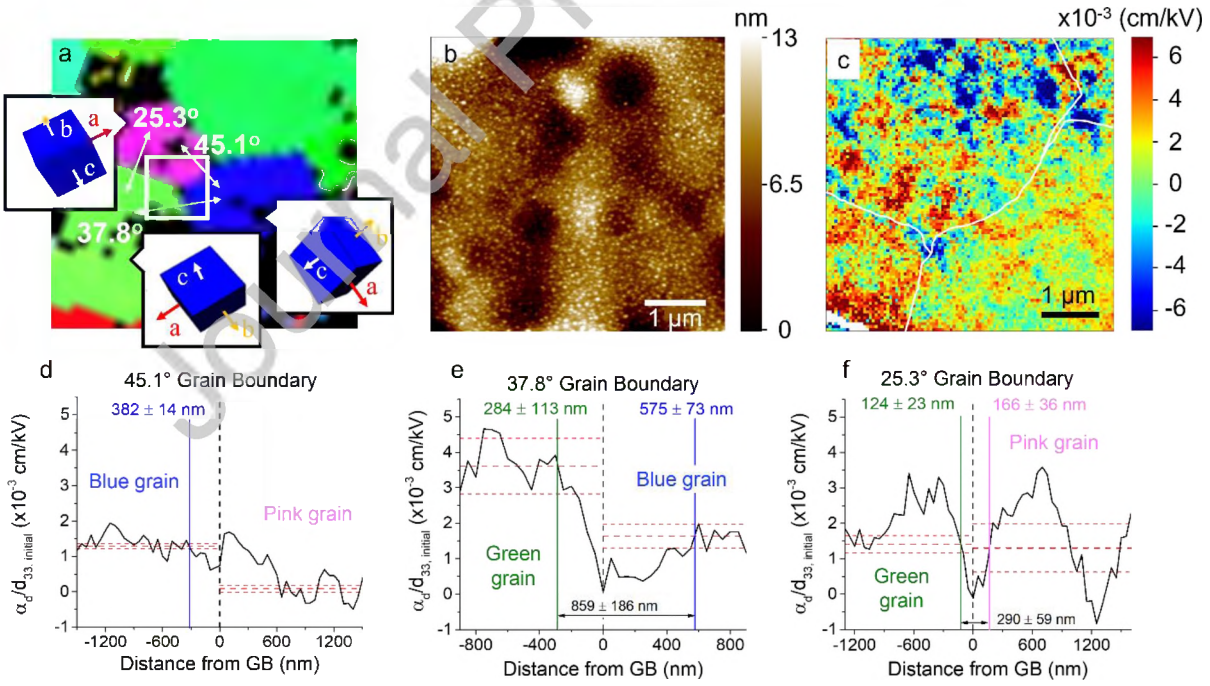

Figure 4: Analysis of the grain boundaries separating the blue/pink/green grains, where all were random grain boundaries. (a) The EBSD schematic (b) topographic 5x5 μm^2 contact AFM scan (c) BE-PFM spectroscopic Rayleigh coefficient ratios and (d-f) the average Rayleigh ratio $\alpha_d/d_{33,initial}$ with respect to grain boundary position for the (d) 45.1° blue/pink grain boundary, (e) 37.8° green/blue grain boundary, and (f) 25.3° green/pink grain boundary.

The random 25.3° boundary was the only investigated boundary that showed a negative value for $\alpha_d/d_{33,initial}$, as seen in Figure 4f. The negative $\alpha_d/d_{33,initial}$ at position zero suggests a non-Rayleigh behavior that could be the result of a non-uniform distribution of restoring forces due to either an anomalously strong pinning site or the absence of domain walls. Assessing whether this difference is correlated with comparatively smaller $SrTiO_3$ grain areas is of interest in future work. Grain sizes were 45 μm^2, 138 μm^2, and 83 μm^2 for pink, green and blue areas, respectively. Figure 4 (d-f) show the pinning distances and width of influence values for the green-blue-pink triple point. Table 1 summarizes the grain boundary angle, width of influence and $\alpha_d/d_{33,initial}$ response at the grain boundary for all nine boundaries in this investigation.

Table 1: Grain boundary (g.b.) angle, total width of influence, and $\alpha_d/d_{33,initial}$ nonlinearity response at the grain boundary for all nine grains boundaries

	CSL Grain Boundary			**Random Grain Boundary**					
g.b. angle (°)	60.9	55.6	29.8	22.5	41.7	13.7	45.1	37.8	25.3
Width of influence (nm)	572 ± 371	285 ± 68	298 ± 55	540 ± 51	905 ± 153	436 ± 216	-	859 ± 186	290 ± 59
$\alpha_d/d_{33,initial}$ at g.b. ($x10^{-3}$ cm/kV)	0.96	2.96	1.93	0.95	0.12	0.94	0.74	0.06	-0.15

Next, the circular width of influence at each triple point location was studied. The radius from the triple point was used as a guideline, and the points at each concentric perimeter were

averaged. An example of a circular radius of influence is shown in Figure 5a for the purple/pink/fuchsia triple point. The BE-PFM nonlinear Rayleigh ratio map is overlain with the grain boundary locations and the approximate radius of influence as a concentric circle around the triple point in white. The radius of influence was determined from data in Figure 5b. It was found that triple points typically serve as deep pinning sites, for which irreversible domain wall motion can be degraded hundreds of nm away on any side of the triple point. At the triple points, the nonlinear piezoelectric response was often non-Rayleigh-like in character, suggesting that the domain walls locally experience a non-Gaussian set of restoring forces or that there are few domain walls at the triple point [23]. The average distance of non-Rayleigh behavior was 220 ± 170 nm in any direction across all investigated triple points; it increased as the number of random grain boundaries increased.

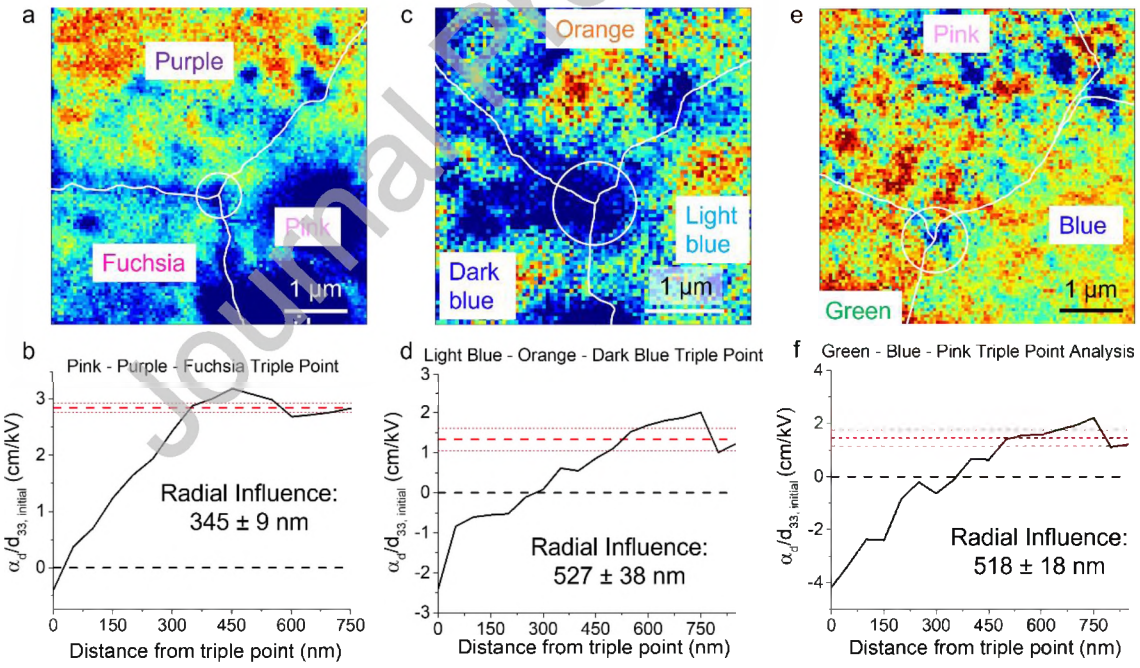

Figure 5: (a) BE-PFM spectroscopic map of $\alpha_d/d_{33,initial}$ Rayleigh ratios for the Purple/Pink/Fuchsia triple point. In white are the grain boundaries and circular width of

influence around the triple point with a radius of 345 ± 9 nm. (b) Rayleigh ratio as a function of the distance away from the triple point in the pink-purple-fuchsia triple point. (c) Light blue-orange-dark blue $\alpha_d/d_{33,initial}$ spectroscopic map with the 527 ± 38 nm radial influence shown and (d) corresponding Rayleigh ratio vs. distance from the triple point. (e) Green-blue-pink triple point spectroscopic map with 518 ± 18 nm radial influence and (f) Rayleigh ratio vs. distance from triple point. The horizontal black lines in (b,d,f) represent the point where $\alpha_d/d_{33,initial}$ becomes positive with respect to the distance. Horizontal red lines represent the mean and 25% of the standard deviation from the mean.

It was found that triple points with a larger number of random boundaries corresponded to deeper minima in $\alpha_d/d_{33,initial}$ and greater distances of non-Rayleigh like behavior. The Pink-Purple-Fuchsia triple point shown in Figure 5a/b had two CSL boundaries. This led to the smallest area of non-Rayleigh behavior and the shallowest minima of the interrogated triple points. Non-Rayleigh behavior was observed for the first 24 nm from the triple point and a radius of influence of 345 ± 9 nm was found. The triple point with one identified CSL boundary is shown in Figure 5c/d; an increased area of non-Rayleigh behavior & deeper minima was observed. Non-Rayleigh behavior was seen up to 279 nm from the triple point and the largest radius of influence of 527 ± 38 nm from the triple point was recorded. This large width of influence is reasonable given the pinning demonstrated by the strongly negative $\alpha_d/d_{33,initial}$ minima. The final triple point, displayed in Figure 5e/f, had no identified CSL boundaries; it showed the lowest recorded $\alpha_d/d_{33,initial}$ minima and the largest area of non-Rayleigh behavior, which was 370 nm. A radius of influence of 518 ± 18 nm from the triple point was determined. The -4.0×10^{-3} cm/kV minima and large distance of non-Rayleigh behavior suggest that increased

pinning from random grain boundaries drove a non-Gaussian set of restoring forces or the absence of domain walls further into the grains.

Previous work has reported correlated motion of domain walls during switching [24], which is consistent with the observation here and elsewhere of correlated motion of domain walls around microstructural features at sub-switching conditions. It is noted that the film-substrate interface tends to produce stronger pinning than the film surface in similar films [25], which is likely to produce some differences from bulk crystals. Moreover, the thin film geometry tends to significantly reduce ferroelastic contributions to the Rayleigh characteristics, relative to bulk crystals and ceramics [5][26]. This is due, at least in part, to the high levels of residual stress inherent in thin films; the residual stresses exceed typical coercive stresses in uncracked films [27]. Thus, it is not straightforward to separate elastic and electrical avalanches, as has been done on bulk crystals [24]. It is not believed that surface roughness plays a significant role in the data measured here, given that the measured surface roughness in the areas measured (discounting surface inclusions not utilized in the analysis) was on the order of a few nanometers, and the PFM measurements sample the entire volume of the film. Nonetheless, it would be interesting to increase the range of the electric field excitation beyond the Rayleigh regime such that the impact of roughness on domain nucleation could be assessed, as has been reported elsewhere [28]. Finally, it will be important in the future to directly measure the domain structures across the grain boundaries imaged here, so that the relative role of domain continuity across different grain boundaries can be directly assessed. Work is on-going to address this point.

In summary, this work provides quantitative measurements of the correlated motion of domain walls at sub-switching conditions in model polycrystalline films. Such data are expected to be useful in modeling the behavior of 3-dimensional ceramic piezoelectrics.

4. Conclusions

The influence of assorted grain boundaries and triple points on the motion of domain walls was studied in $PbZr_{0.52}Ti_{0.48}O_3$ films. It was found that the character of the grain boundary affected the way in which domain walls moved. In particular, coincident site lattice grain boundaries exhibited shallower minima in $\alpha_d/d_{33,initial}$ than was observed for random grain boundaries. It is speculated that regularity in the crystalline arrangement of the two grains may facilitate collective domain wall movement between grains. In contrast, a triple point with three random boundaries exacerbated pinning and contributed to low $\alpha_d/d_{33,initial}$ minima. The width of influence on domain wall motion scaled better with the difference between the minima and the steady state $\alpha_d/d_{33,initial}$ than it did with the value of $\alpha_d/d_{33,initial}$ at the grain boundary. That is, wider widths of influence were observed with larger differences between the minima and the steady state $\alpha_d/d_{33,initial}$. Different grain boundaries influenced the mobility of domain walls on length scales from 124 ± 23 nm to 905 ± 153 nm normal to their respective grain boundary. The largest width of influence (905 ± 153 nm) occurred in the triple point with zero CSL boundaries, while the largest recorded width of influence for a CSL boundary was 572 nm. Further studies in static domain structures around random and CSL boundaries with different shared rotation axes is of interest.

This study also provides the first quantitative measurements of the effects of triple points on the motion of domain walls. It was found that immediately adjacent to the triple points, a region of material which did not show Rayleigh-like characteristics was observed, i.e. $\alpha_d/d_{33,initial}$ was negative. This could be a result of either a non-Gaussian distribution of restoring forces (perhaps due to very strong pinning associated with the triple point itself) and/or a reduction in the number of domain walls at the triple point. At larger diameters, a region of material with suppressed (but positive) $\alpha_d/d_{33,initial}$ was observed, before the material reached steady state at still longer

distances. As the number of random boundaries within a given triple point is increased, the distance from the triple point where Rayleigh-like behavior occurs increased and the radial influence of the triple point on domain wall motion also increased.

5. Acknowledgements

This work was supported by The National Science Foundation [grant number NSF DMR-2025439]. PFM research was supported by the Center for Nanophase Materials Sciences (CNMS), which is a US Department of Energy, Office of Science User Facility at Oak Ridge National Laboratory. $SrTiO_3$ substrates were provided by Dr. Sridar Venigalla.

6. References

[1] A. Pramanick, D. Damjanovic, J.E. Daniels, J.C. Nino, J.L. Jones, Origins of electro-mechanical coupling in polycrystalline ferroelectrics during subcoercive electrical loading, J. Am. Ceram. Soc. 94 (2011) 293–309. https://doi.org/10.1111/j.1551-2916.2010.04240.x.

[2] D.A. Hall, Nonlinearity in piezoelectric ceramics, J. Mater. Sci. 36 (2001) 4575–4601.

[3] Q.M. Zhang, H. Wang, N. Kim, L.E. Cross, Direct evaluation of domain-wall and intrinsic contributions to the dielectric and piezoelectric response and their temperature dependence on lead zirconate-titanate ceramics, J. Appl. Phys. 75 (1994) 454–459. https://doi.org/10.1063/1.355874.

[4] D. Damjanovic, M. Demartin, The Rayleigh law in piezoelectric ceramics, J. Phys. D. Appl. Phys. 29 (1996) 2057–2060. https://doi.org/10.1088/0022-3727/29/7/046.

[5] N. Bassiri-Gharb, I. Fujii, E. Hong, S. Trolier-McKinstry, D. V. Taylor, D. Damjanovic, Domain wall contributions to the properties of piezoelectric thin films, J. Electroceramics. 19 (2007) 47–65. https://doi.org/10.1007/s10832-007-9001-1.

[6] C.A. Randall, N. Kim, J.P. Kucera, W. Cao, T.R. Shrout, Intrinsic and extrinsic size effects in fine-grained morphotropic-phase-boundary lead zirconate titanate ceramics, J. Am. Ceram. Soc. 81 (1998) 677–688. https://doi.org/10.1111/j.1151-2916.1998.tb02389.x.

[7] F. Griggio, S. Trolier-McKinstry, Grain size dependence of properties in lead nickel niobate-lead zirconate titanate films, J. Appl. Phys. 107 (2010). https://doi.org/10.1063/1.3284945.

[8] W. Cao, C.A. Randall, Grain size and domain size relations in bulk ceramic ferroelectric materials, J. Phys. Chem. Solids. 57 (1996) 1499–1505. https://doi.org/10.1016/0022-3697(96)00019-4.

[9] G. Arlt, The influence of microstructure on the properties of ferroelectric ceramics, Ferroelectrics. 104 (1990) 217–227. https://doi.org/10.1080/00150199008223825.

[10] A. Gruverman, O. Auciello, H. Tokumoto, Nanoscale investigation of fatigue effects in $Pb(Zr,Ti)O_3$ films, Appl. Phys. Lett. 69 (1996) 3191–3193. https://doi.org/10.1063/1.117957.

[11] S. Choudhury, Y.L. Li, C. Krill, L.Q. Chen, Effect of grain orientation and grain size on ferroelectric domain switching and evolution: Phase field simulations, Acta Mater. 55 (2007) 1415–1426. https://doi.org/10.1016/j.actamat.2006.09.048.

[12] D.M. Marincel, H.R. Zhang, J. Britson, A. Belianinov, S. Jesse, S. V. Kalinin, L.Q. Chen, W.M. Rainforth, I.M. Reaney, C.A. Randall, S. Trolier-McKinstry, Domain pinning near a single-grain boundary in tetragonal and rhombohedral lead zirconate titanate films, Phys. Rev. B - Condens. Matter Mater. Phys. 91 (2015) 1–12. https://doi.org/10.1103/PhysRevB.91.134113.

[13] D.M. Marincel, H. Zhang, S. Jesse, A. Belianinov, M.B. Okatan, S. V. Kalinin, W.M. Rainforth, I.M. Reaney, C.A. Randall, S. Trolier-McKinstry, Domain wall motion across various grain boundaries in ferroelectric thin films, J. Am. Ceram. Soc. 98 (2015) 1848–1857. https://doi.org/10.1111/jace.13535.

[14] S. Tsurekawa, K. Ibaraki, K. Kawahara, T. Watanabe, The continuity of ferroelectric domains at grain boundaries in lead zirconate titanate, Scr. Mater. 56 (2007) 577–580. https://doi.org/10.1016/j.scriptamat.2006.12.029.

[15] S. Mantri, J. Oddershede, D. Damjanovic, J.E. Daniels, Ferroelectric domain continuity over grain boundaries, Acta Mater. 128 (2017) 400–405. https://doi.org/10.1016/j.actamat.2017.01.065.

[16] J. Fousek, Permissible domain walls in ferroelectric species, Czechoslov. J. Phys. B. 21 (1971) 955–968.

[17] J. Sapriel, Domain-wall orientations in ferroelastics, Phys. Rev. B. 12 (1975) 5128–5140.

[18] T.M. Borman, {001} Textured growth of doped, gradient free, lead zirconate titanate thin films by chemical solution deposition, The Pennsylvania State University, 2016.

[19] W. Zhu, I. Fujii, W. Ren, S. Trolier-McKinstry, Domain wall motion in A and B site donor-doped $Pb(Zr_{0.52}Ti_{0.48})O_3$ films, J. Am. Ceram. Soc. 95 (2012) 2906–2913. https://doi.org/10.1111/j.1551-2916.2012.05243.x.

[20] S. Jesse, S. V. Kalinin, R. Proksch, A.P. Baddorf, B.J. Rodriguez, The band excitation method in scanning probe microscopy for rapid mapping of energy dissipation on the nanoscale, Nanotechnology. 18 (2007). https://doi.org/10.1088/0957-4484/18/43/435503.

[21] P. Bintachitt, S. Jesse, D. Damjanovic, Y. Han, I.M. Reaney, S. Trolier-McKinstry, S. V. Kalinin, Collective dynamics underpins Rayleigh behavior in disordered polycrystalline

ferroelectrics, Proc. Natl. Acad. Sci. U. S. A. 107 (2010) 7219–7224. https://doi.org/10.1073/pnas.0913172107.

[22] F. Griggio, S. Jesse, A. Kumar, D.M. Marincel, D.S. Tinberg, S. V. Kalinin, S. Trolier-McKinstry, Mapping piezoelectric nonlinearity in the Rayleigh regime using band excitation piezoresponse force microscopy, Appl. Phys. Lett. 98 (2011) 98–101. https://doi.org/10.1063/1.3593138.

[23] T. O'Reilly, K. Holsgrove, A. Gholinia, D. Woodruff, A. Bell, J. Huber, M. Arredondo, Exploring domain continuity across $BaTiO_3$ grain boundaries: Theory meets experiment., Acta Mater. 235 (2022) 118096. https://doi.org/10.1016/j.actamat.2022.118096.

[24] Y. Xu, G. Shao, J. Pang, Y. Zhou, X. Ding, J. Sun, T. Lookman, E.K.H. Salje, D. Xue, Avalanches during ferroelectric and ferroelastic switching in barium titanate ceramics, Phys. Rev. Mater. 6 (2022) 124413. https://doi.org/10.1103/PhysRevMaterials.6.124413.

[25] L.M. Denis-Rotella, G. Esteves, J. Walker, H. Zhou, J.L. Jones, S. Trolier-McKinstry, Residual stress and ferroelastic domain reorientation in declamped {001} $Pb(Zr_{0.3}Ti_{0.7})O_3$ films, IEEE Trans. Ultrason. Ferroelectr. Freq. Control. 68 (2021) 259–272. https://doi.org/10.1109/TUFFC.2020.2987438.

[26] N. Bassiri-Gharb, S. Trolier-McKinstry, D. Damjanovic, Strain-modulated piezoelectric and electrostrictive nonlinearity in ferroelectric thin films without active ferroelastic domain walls, J. Appl. Phys. 110 (2011). https://doi.org/10.1063/1.3665410.

[27] F. Griggio, S. Jesse, A. Kumar, O. Ovchinnikov, H. Kim, T.N. Jackson, D. Damjanovic, S. V. Kalinin, S. Trolier-McKinstry, Substrate clamping effects on irreversible domain wall dynamics in lead zirconate titanate thin films, Phys. Rev. Lett. 108 (2012) 1–5. https://doi.org/10.1103/PhysRevLett.108.157604.

[28] G. Lu, S. Li, X. Ding, J. Sun, E.K.H. Salje, Ferroelectric switching in ferroelastic materials with rough surfaces, Sci. Rep. 9 (2019) 1–7. https://doi.org/10.1038/s41598-019-52240-3.

Graphical abstract

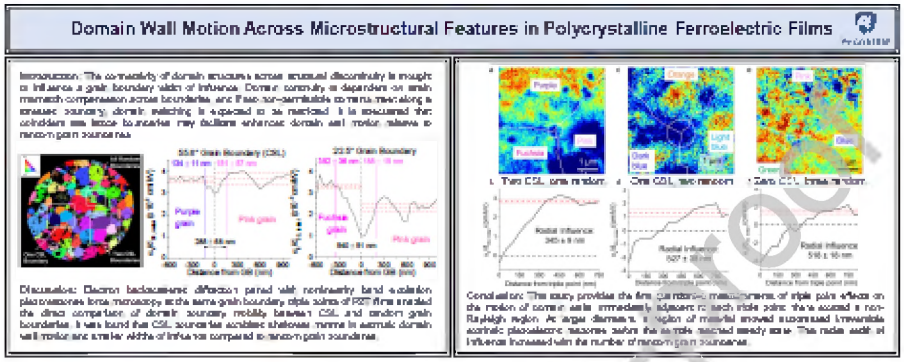

Declaration of interests

☒The authors declare that they have no known competing financial interests or personal relationships that could have appeared to influence the work reported in this paper.

☐The authors declare the following financial interests/personal relationships which may be considered as potential competing interests: